Journal for ImmunoTherapy of Cancer

Preventing surgery-induced natural killer cell suppression and metastases by inhibiting PI3K-gamma signaling in myeloid-derived suppressor cells

Leonard Angka ,[1,2] Gayashan Tennakoon ,[1,2] David P Cook,[1,3] Andre B Martel,[1,4] Marisa Market ,[1,2] Christiano Tanese de Souza,[1] Emma Cummins,[5] Ismael Samudio,[5] Natasha Kekre ,[1] Michele Ardolino ,[1,2] Barbara C Vanderhyden ,[1,3] Michael A Kennedy,[1] Rebecca C Auer [1,4]

To cite: Angka L, Tennakoon G, Cook DP, *et al*. Preventing surgery-induced natural killer cell suppression and metastases by inhibiting PI3K-gamma signaling in myeloid-derived suppressor cells. *Journal for ImmunoTherapy of Cancer* 2026;**14**:e013304. doi:10.1136/jitc-2025-013304

► Additional supplemental material is published online only. To view, please visit the journal online (https://doi.org/10.1136/jitc-2025-013304).

LA and GT contributed equally.

Accepted 16 January 2026

For numbered affiliations see end of article.

Correspondence to
Dr Rebecca C Auer;
rauer@ohri.ca

ABSTRACT

Background Myeloid-derived suppressor cells (MDSCs) have a dominating presence in the postoperative period, mediating the suppression of natural killer (NK) cells and promoting cancer metastases after surgery. However, their phenotype and effects on postoperative cellular immunity remain incompletely understood. This study aims to functionally characterize surgery-induced (sx) MDSCs and identify potential therapeutic strategies to mitigate their immunosuppressive effects.

Methods We used multicolor flow cytometry to characterize sx-MDSCs from n=55 patients with cancer undergoing surgery at various time points. Furthermore, single-cell RNA sequencing was performed on a cohort of patients. Our functional ex vivo sx-MDSC:NK cell suppression assay was used to investigate the activity of sx-MDSCs and to screen a 147 small molecule library to identify sx-MDSC antagonists. Lastly, we used preclinical murine models of postoperative metastases to evaluate the therapeutic potential of the inhibitors identified.

Results Sx-MDSCs significantly expanded after surgery and single-cell RNA sequencing identified signatures resembling immunosuppressive monocytes, including an upregulation of PI3K signaling. These sx-MDSCs also suppressed NK cell activity from patient samples and the small molecule screen identified PI3K-γ inhibitors as potent modulators of sx-MDSC activity. In our murine models, inhibiting PI3K-γ with specific inhibitors reduced postoperative metastases, further corroborating the role of this pathway in sx-MDSC-mediated immune suppression.

Conclusions Our findings highlight the critical role of PI3K-γ signaling in postoperative sx-MDSC-mediated immune suppression. Targeting this pathway with PI3K-γ inhibitors represents a promising therapeutic strategy to prevent NK cell suppression and reduce postoperative metastases.

WHAT IS ALREADY KNOWN ON THIS TOPIC

⇒ Surgery-induced myeloid-derived suppressor cells (sx-MDSCs) accumulate in the postoperative period following tumor resection, mediating suppression of natural killer (NK) cells and contributing to metastatic recurrence. However, their phenotype and mechanisms of their suppressive activity remain incompletely characterized.

WHAT THIS STUDY ADDS

⇒ We identified PI3K-γ as a central mediator of sx-MDSC suppressive activity. Inhibition of PI3K-γ in sx-MDSCs preserved NK cell function and significantly reduced metastatic recurrence in preclinical models. This study establishes the PI3K-γ pathway as a therapeutic target for mitigating postoperative immune suppression.

HOW THIS STUDY MIGHT AFFECT RESEARCH, PRACTICE OR POLICY

⇒ These findings provide a strong rationale for developing perioperative interventions targeting sx-MDSCs to reduce metastatic recurrence following cancer surgery. PI3K-γ inhibition represents a novel therapeutic strategy that could be implemented in the preoperative or early postoperative period. Future work could leverage these findings to investigate targeted delivery platforms, such as antibody-drug conjugates directed against sx-MDSC-specific markers, to maximize therapeutic efficacy while minimizing systemic toxicity.

BACKGROUND

Surgical resection with curative intent remains the standard and often most effective treatment for patients with localized solid malignancies. However, even after complete tumor removal and years with no evidence of disease, a substantial proportion of patients ultimately experience metastatic recurrence within 5 years of surgery. The presence of circulating tumor cells prior to surgical resection is a strong predictor of postoperative recurrence.[1] This suggests that minimal residual disease can persist despite curative surgery and may proliferate during the

profound period of antitumor immune suppression that follows the procedure. Postoperative immune suppression after surgery can negatively impact a patient's susceptibility to infections and likelihood of metastatic relapse.[2]

During surgery, the disruption of endothelial cell barriers causes the release of damage-associated molecular patterns (DAMPs), or "alarmins", to alert and mobilize immune cells to the site of surgery to remove damaged cells and protect from foreign pathogens.[3] Monocytes that are recruited immediately from bone marrow reserves release inflammatory cytokines such as interleukin (IL)-1, IL-6 and tumor necrosis factor (TNF)-α. While monocytes and neutrophils mainly mediate the initial proinflammatory response, they are also critical for its resolution.[3] To compensate for the large egress of monocytes, the body activates emergency myelopoiesis, resulting in a rapid release of immature myeloid cells.[4]

These immature myeloid cells are anti-inflammatory and immunosuppressive-like cells with altered cytokine profiles (e.g. IL-10 and transforming growth factor-beta (TGF-β) secretion) and reduced antigen presentation (downregulation of Human Leukocyte Antigen - DR isotype (HLA-DR)). Phenotypically and functionally, they resemble myeloid-derived suppressor cells (MDSCs) and have been implicated in mediating postoperative immunosuppression.[5–7] The impact of these immature myeloid cells on recovery from surgery and sepsis has been studied, but very little is known about their effect on recurrence following cancer surgery.

The central role of the immune system, particularly natural killer (NK) cells,[8] in metastatic disease control is well recognized. Immune suppression following surgery is several folds higher than immune suppression induced by the cancer itself,[9] and serves as a predictor of metastatic cancer recurrences.[7 10 11] Our group has shown in murine studies that NK and T-cell suppression in the early postoperative period is responsible for cancer recurrence and metastases.[12–14] We have confirmed that "surgery-induced" (sx)-MDSCs are responsible for postoperative immune suppression.[13]

To effectively target postoperative immune suppression by sx-MDSCs, proper characterization is essential. MDSCs are described as being either polymorphonuclear (PMN-), monocytic (M-), or early stage (E-) MDSCs.[15 16] However, the phenotypic markers defining these subtypes often overlap, complicating their classification.[16] The key defining feature of MDSCs remains their ability to suppress immune effector cells, particularly NK cells and T cells.[7 10 12]

In this study, we used multicolor flow cytometry and single-cell RNA sequencing (scRNA-seq) to phenotypically characterize postoperative sx-MDSCs. Using a functional ex vivo co-culture suppression assay, we confirmed these cells suppress NK cell effector functions. Using this assay, we screened a small molecule library to identify molecules that can prevent sx-MDSC suppression. This led us to identify PI3K-γ as the key signaling pathway governing their suppressive machinery. Furthermore, we demonstrated that targeting this pathway can attenuate postoperative NK cell suppression and cancer metastases.

Table 1 Patient demographics for flow cytometry

Category	Subcategory	Patients with cancer (n=55)	Healthy (n=6)
Sex	Male (n)	30	4
	Female (n)	25	2
Age - median; range		64; 29–81	30; 28–42
	<50 years (n)	8	6
	50–69 years (n)	33	0
	>70 years (n)	14	0
Cancer type - n	GI	15	N/A
	GU	14	
	Prostate	12	
	Lung	9	
	Sarcoma	4	
	Neuroendocrine	1	
Cancer stage - n (%)	Stage 0 (in situ)	10	N/A
	Stage 1	14	
	Stage 2	16	
	Stage 3	13	
	Stage 4	2	
Length of operation - median; range		3.5; 2–10	N/A

GI, gastrointestinal (upper and lower GI and pancreatic cancer); GU, genitourinary (kidney, bladder, ureteral, uterine/endometrial).

RESULTS

Surgery-induced myeloid-derived suppressor cells in patients with cancer

The expansion and persistence of immature myeloid cells in the postoperative period has been observed and reported previously.[7 13] To corroborate these findings, we assessed a cohort of cancer surgery patients (n=55; table 1) from various cancer types, procedures, sex and ages for changes in immune cell proportions immediately following surgery (postoperative day 1; POD1) using a harmonized multicolor flow cytometry panel for human MDSCs[15] (figure 1A,B; online supplemental figures S1 and S2). We focused our analysis on the expansion and characterization of myeloid cells ($CD33^{+}Lin^{-}$), which are elevated prior to surgery in patients with cancer compared with healthy volunteers and had significantly increased by 1.9-fold on POD1 (figure 1C, p<0.0001).

In humans, MDSCs are categorized into M-MDSC ($CD14^{+}CD15^{lo}HLA\text{-}DR^{lo}$), PMN-MDSC ($CD14^{-}CD15^{hi}HLA\text{-}DR^{-}$), or E-MDSCs ($CD14^{-}CD15^{-}$).[15 16] In our cancer surgery cohort, the M-MDSC and PMN-MDSC subtypes

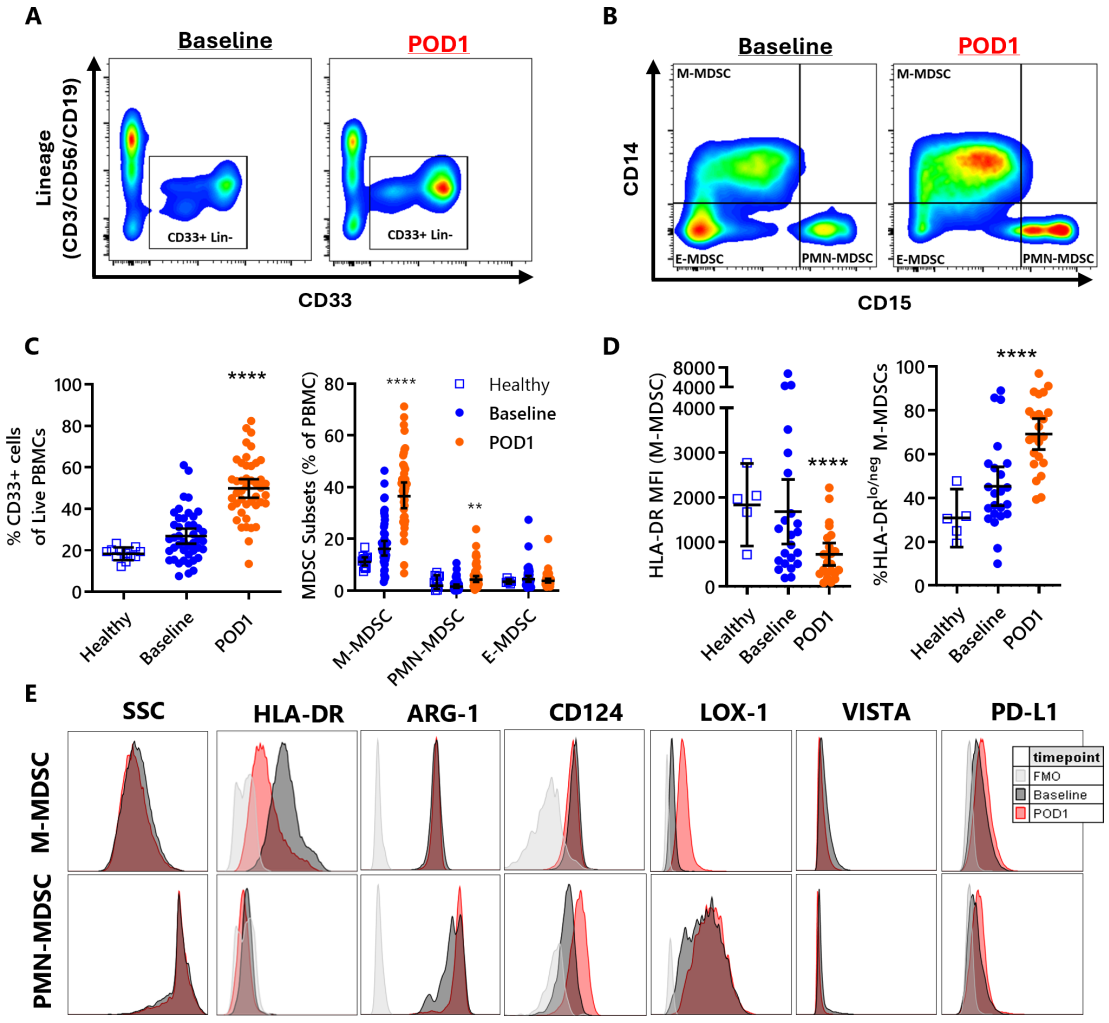

Figure 1 Large expansion of phenotypically defined sx-MDSCs comprised mainly of M-MDSC and PMN-MDSCs immediately after surgery (POD1). (A) Representative flow plots showing CD33 versus Lineage (CD3/CD56/CD19) for baseline (left) and POD1 (right) PBMCs. (B) Representative flow plots gated down on $CD33^{+}Lin^{-}$ cells showing CD15 versus CD14 expression. (C) Healthy controls (n=15), Baseline, and POD1 patients (n=44) proportion of $CD33^{+}Lin^{-}$ cells (left) and MDSC subsets (right). (D) The MFI of HLA-DR gated on M-MDSCs (left) and the proportion of M-MDSCs that are $HLA\text{-}DR^{lo}$ (right) in healthy controls, baseline and POD1 patients with cancer. (E) Representative histograms of common M-MDSC and PMN-MDSC markers, before and after surgery. Statistical analysis was performed using Wilcoxon matched pairs signed-rank test or Kruskal-Wallis with Dunn's post test. **** $p \leq 0.0001$. FMO, fluorescence minus one control; HLA-DR, human leukocyte antigen - DR isotype; E-MDSC, early stage-MDSC; M-MDSC, monocytic-MDSC; MDSC, myeloid derived suppressor cell; sx-MDSC, surgery-induced MDSC, MFI; mean fluorescence instensity; PBMC, peripheral blood mononuclear cell; PMN-MDSC, polymorphonuclear-MDSC; POD1, postoperative day 1.

expanded 2.1-fold and 2.9-fold, respectively, and there was no observed change in the frequency of E-MDSCs after surgery (figure 1C). The majority of sx-MDSCs on POD1 were M-MDSCs, which accounted for 39.6% (95% CI 34.8% to 44.5%) of PBMCs, while PMN-MDSCs and E-MDSCs accounted for 6.0% (95% CI 4.2% to 8.0%) and 4.4% (95% CI 3.3% to 5.5%), respectively. On POD1, a significant decrease in the mean fluorescence intensity (MFI) of HLA-DR on M-MDSCs was observed, decreasing from an average MFI of 1677–724 ($p<0.0001$), and the proportion of $HLA\text{-}DR^{lo}$ M-MDSCs increased significantly from 40% to 66% ($p<0.0001$) (figure 1D, online supplemental figure S1).

We also assessed the effect of surgery on MDSC-specific markers such as arginase-1 (Arg1), CD124 (IL-4Rα),[15] and Lox-1,[17] as well as exploratory immune checkpoint markers VISTA[18] and PD-L1.[19] Although M-MDSCs and PMN-MDSCs have different levels of expression for these markers, they did not significantly increase after surgery (figure 1E). Next, we wanted to confirm the suppressive functions of the different sx-MDSC subtypes.

Sx-MDSCs isolated from cancer patients on POD1 (online supplemental figure S3) and co-cultured with NK92-MI cells suppressed NK cell cytotoxicity against K562 target tumor cells (figure 2A,B). This was not due to NK92-MI cells targeting the $CD33^{+}$ cells because the viability of $CD33^{+}$ cells was not affected following 6-hour or 24-hour co-cultures with NK92-MI alone (figure 2B) nor was this due to $CD33^{+}$ cells reducing NK92-MI cell viability (data not shown). Sx-MDSCs on POD1 had greater NK

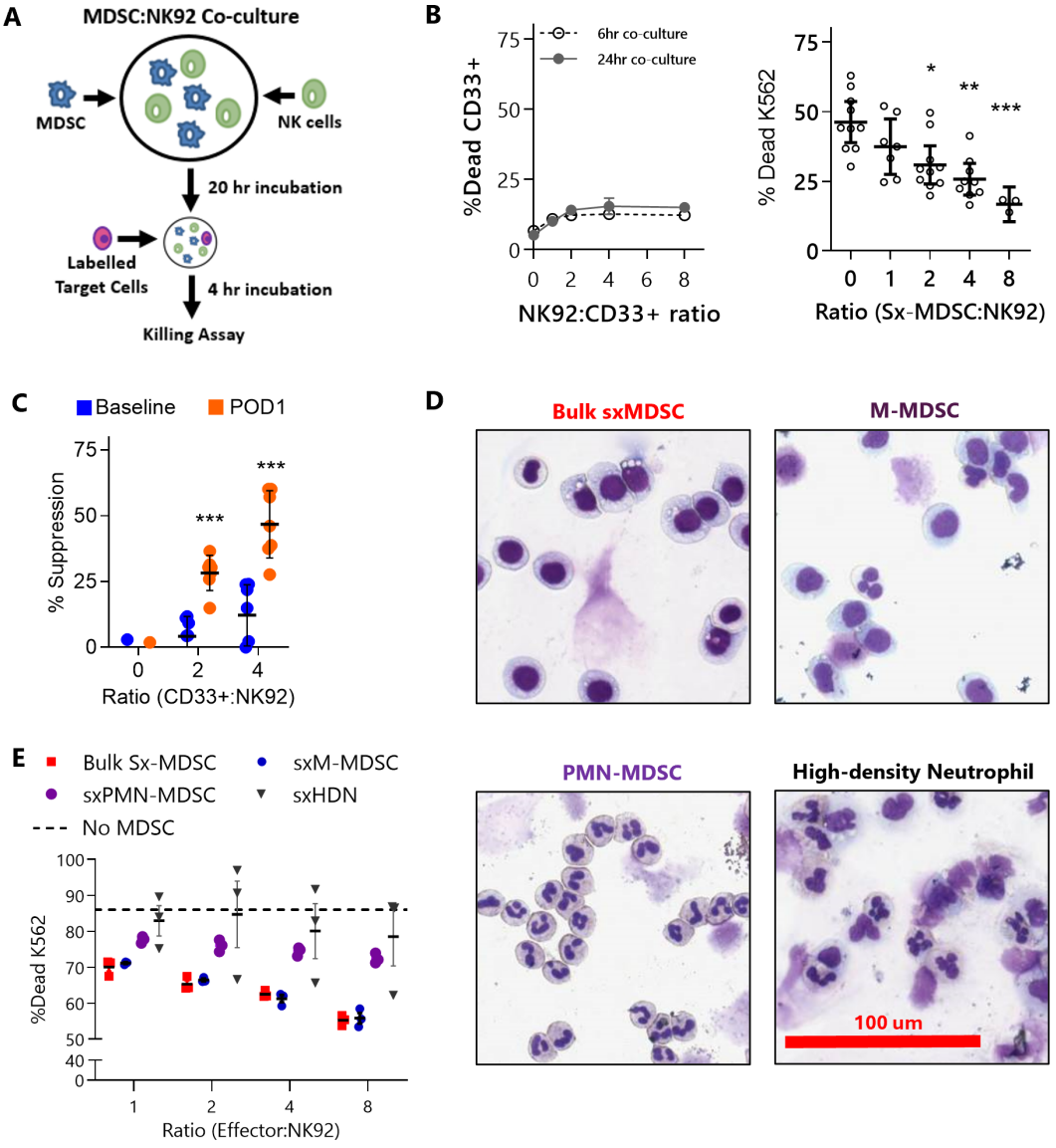

Figure 2 Sx-MDSCs suppress NK92-MI cytotoxicity. (A) Schematic of MDSC-NK92 co-culture suppression assay with CP450-labeled K562 target cells. (B) NK92-MIs were co-cultured at increasing ratios with CD33+ cells for 6 or 24 hours (in the absence of K562s) to assess CD33+ cell death by NK92-MI (left). Sx-MDSCs from POD1 patient samples (n=10) were co-cultured with NK92-MI cells and NK cytotoxicity was measured as % dead K562 (right). (C) % suppression was calculated as the reduction of NK cytotoxicity, normalized to NK cells alone (ratio=0). CD33+ cells isolated from baseline and patient-matched POD1 blood were co-cultured with NK92-MI and K562 targets to measure their suppressive capacity (n=5). (D) Representative images of sorted cells stained with Giemsa Wright. (E) Bulk Sx-MDSCs, M-MDSCs, PMN-MDSCs, and HDN from POD1 patients (n=3) co-cultured with NK92-MI to measure effect on NK cytotoxicity. The NK92-MI alone control group is indicated by the broken horizontal line. Statistical analysis used Kruskal-Wallis with Dunn's post-test. ****p≤0.0001. HDN, high-density neutrophils; M-MDSC, monocytic-MDSC; MDSC, myeloid-derived suppressor cell; NK, natural killer; sx-MDSC, surgery-induced MDSC, PMN-MDSC, polymorphonuclear-MDSC; POD1, postoperative day 1.

cell suppression compared with MDSCs isolated at baseline (figure 2C). To determine the suppressive capacity of different MDSC subsets, we isolated PMN-MDSCs, M-MDSCs, and also high-density neutrophils (HDNs) on POD1 (figure 2D, online supplemental figure S3) and co-cultured these cells with NK92-MI cells. Sx-M-MDSCs suppressed NK cell cytotoxicity to the same extent as bulk-MDSCs, while sx-PMN-MDSCs only partially suppressed. Notably, sx-HDNs did not result in any suppression (figure 2E). Therefore, on POD1, sx-MDSCs are a mixture of sx-M-MDSC (majority) and sx-PMN-MDSC (minority) subsets with different phenotypic features, and sx-M-MDSCs are the primary drivers of NK cell suppression.

Single-cell RNA sequencing captures significant transcriptional perturbations in monocytes after surgery resembling immunosuppressive MDSCs

To understand the transcriptional changes occurring in the myeloid population after surgery, we performed scRNA-seq on cryopreserved peripheral blood

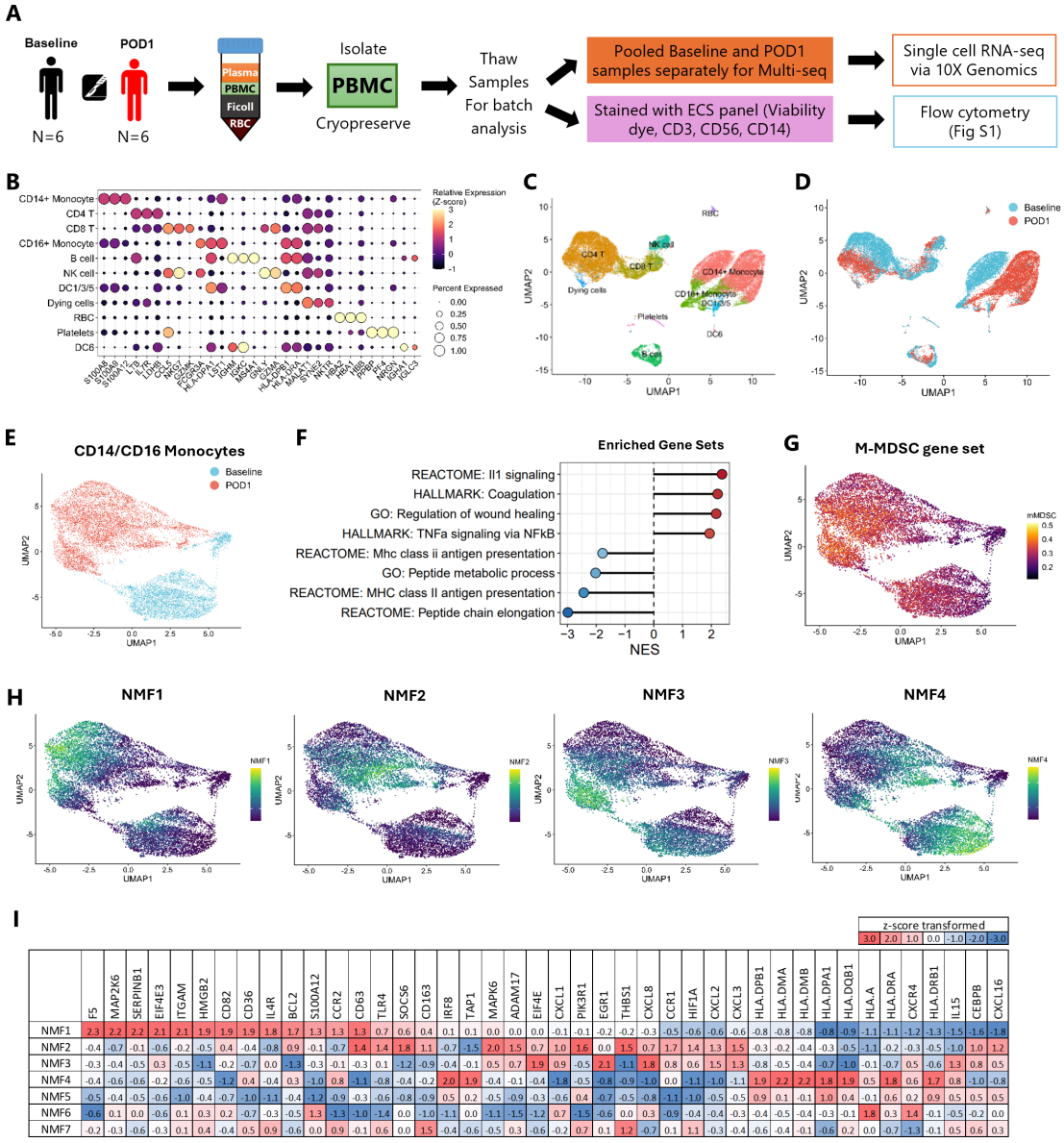

	F5	MAP2K6	SERPINB1	EIF4E3	ITGAM	HMGB2	CD82	CD36	IL4R	BCL2	S100A12	CCR2	CD63	TLR4	SOCS6	CD163	IRF8	TAP1	MAPK6	ADAM17	EIF4E	CXCL1	PIK3R1	EGR1	THBS1	CXCL8	CCR1	HIF1A	CXCL2	CXCL3	HLA.DPB1	HLA.DMA	HLA.DMB	HLA.DPA1	HLA.DQB1	HLA.A	HLA.DRA	CXCR4	HLA.DRB1	IL15	CEBPB	CXCL16
NMF1	2.3	2.2	2.2	2.1	2.1	1.9	1.9	1.9	1.8	1.7	1.3	1.3	1.3	0.7	0.6	0.4	0.1	0.1	0.0	0.0	0.0	-0.1	-0.1	-0.2	-0.2	-0.3	-0.5	-0.6	-0.6	-0.6	-0.8	-0.8	-0.8	-0.8	-0.9	-1.1	-1.1	-1.2	-1.3	-1.5	-1.6	-1.8
NMF2	-0.4	-0.7	-0.1	-0.6	-0.2	-0.5	0.4	-0.4	-0.8	0.9	-0.1	-0.7	1.4	1.4	1.8	1.1	-0.7	-1.5	2.0	1.5	0.7	1.0	1.6	0.0	1.5	0.7	1.7	1.4	1.3	1.5	-0.3	-0.2	-0.4	-0.3	-0.5	-1.1	-0.2	-0.3	-0.5	-1.0	1.0	1.2
NMF3	-0.3	-0.4	-0.5	0.3	-0.5	-1.1	-0.2	-0.7	0.0	-1.3	-0.3	-0.1	-0.3	0.1	-1.2	-0.9	-0.4	-0.1	0.5	0.7	1.9	0.9	-0.5	2.1	-1.1	1.8	0.8	0.6	1.5	1.3	-0.8	-0.5	-0.4	-0.7	-1.0	-0.1	-0.7	0.5	-0.6	1.3	0.8	0.5
NMF4	-0.4	-0.6	-0.6	-0.2	-0.6	-0.5	-1.2	0.4	-0.4	0.3	-1.0	0.8	-1.1	-0.8	-0.4	-0.2	2.0	1.9	-0.4	-0.1	-0.4	-1.8	-0.5	-0.8	-0.9	-1.0	0.0	-1.1	-1.0	-1.1	1.9	2.2	2.2	1.8	1.9	0.5	1.8	0.6	1.7	0.8	-1.0	-0.8
NMF5	-0.5	-0.4	-0.5	-0.6	-1.0	-0.4	-0.7	-1.0	-1.1	-0.4	-1.2	-0.9	-0.3	-0.6	-0.8	-0.9	0.5	0.2	-0.5	-0.9	-0.3	-0.6	0.4	-0.7	-0.5	-0.8	-1.1	-1.0	-0.5	-0.5	0.9	0.1	-0.1	1.0	0.4	-0.1	0.6	0.2	0.9	0.5	0.5	0.5
NMF6	-0.6	0.1	0.0	-0.6	0.1	0.3	0.2	-0.7	-0.3	-0.5	1.3	-1.3	-1.0	-1.4	0.0	-1.0	-1.1	0.0	-1.1	-1.5	-1.2	0.7	-1.5	-0.6	0.0	0.3	-0.9	-0.4	-0.4	-0.3	-0.4	-0.5	-0.4	-0.3	-0.1	1.8	0.3	1.4	-0.1	-0.5	-0.2	0.0
NMF7	-0.2	-0.3	-0.6	-0.3	0.1	0.4	-0.4	0.5	0.9	-0.6	0.0	0.9	-0.1	0.6	0.0	1.5	-0.4	-0.6	-0.5	0.3	-0.6	-0.2	0.7	0.1	1.2	-0.7	0.1	1.1	-0.3	-0.4	-0.6	-0.4	-0.1	-0.6	0.2	0.0	-0.7	-1.3	-0.1	0.5	0.6	0.3

Figure 3 scRNA-seq of cryopreserved PBMCs before and after surgery reveals drastically altered monocyte/myeloid cell expression profiles on POD1. (A) Schematic showing PBMCs (cryopreserved) from six matched baseline and POD1 patients were processed for multiplexed scRNA-seq with the 10x Genomics Chromium platform. (B) Dot plot displaying the relative expression of the top three marker genes (x-axis) of each cluster (y-axis). (C) UMAP plot of scRNA-seq data. Each point corresponds to a single cell and is colored by cluster. (D) Identical UMAP embedding as in (C), with Baseline and POD1 cells labeled. (E) UMAP plot of the CD14+ and CD16+ monocyte population at baseline and POD1. (F) GSEA showing the NES of the top upregulated and downregulated pathways. All gene sets are significantly enriched (FDR<0.05). (G) UMAP plot showing activity of an M-MDSC gene set from Alshetaiwai *et al*; in monocyte populations in Baseline and POD1 samples. (H) NMF plots of gene expression programs for NMF 1, 2, 3 and 4 (see online supplemental figure S5 for all NMF programs). (I) A heatmap of selected genes driving the various NMF gene expression programs (z-score transformed; ranked according to NMF1). FDR, false discovery rate; GSEA, gene set enrichment analysis; M-MDSC, monocytic-myeloid-derived suppressor cell; NES, normalized enrichment scores; NMF, non-negative matrix factorization; PBMC, peripheral blood mononuclear cell; POD1, postoperative day 1; scRNA-seq, single-cell RNA sequencing; UMAP, uniform manifold approximation and projection.

mononuclear cell (PBMCs) from matched baseline and POD1 patient samples (n=6) (figure 3A; online supplemental figure S4 and table S1). After removing cells with low gene detection (<200 detected genes) and high mitochondrial gene content (>25%), we integrated and clustered the remaining 30,773 cells by underlying cell type (figure 3B), resulting in the identification of 10 cell types (figure 3C,D). Interestingly, we observed reproducible shifts in the transcriptional profiles of all immune cell types after surgery. Although there were no differences on POD1 in the proportion of NK cells (p=0.8), there was a significant decrease in the %CD3+cells (0.6-fold change, p=0.03) and increase in the %CD14+monocytes (2.0-fold change, p=0.3) of PBMCs measured by flow cytometry

(online supplemental figure S4B–D). As the monocytic sx-MDSCs make up the majority of the PBMCs postoperatively (online supplemental figure S4D, figure 3D and E), we performed differential expression[20] followed by Gene Set Enrichment Analysis (GSEA) using a collection of query gene sets from the Molecular Signatures Database (gene ontology, GO terms; Kyoto encyclopedia of genes and genomes, KEGG pathways; Reactome pathways; and Hallmark gene sets)[21 22] on the monocytic populations. This revealed an upregulation of expected/known responses to surgery such as IL-1 signaling, coagulation, and wound healing (figure 3F). Interestingly, there was an increase in the "TNF-α signalling via NF-κB" Hallmark gene set which has been described to be upregulated in immunosuppressive monocytes and MDSCs.[23] Furthermore, the downregulation of the Reactome pathway "MHC class II antigen presentation" has been described previously[24] and supports our flow cytometry observations of HLA-DR (figure 1D).

Although the monocyte clusters separated into two distinct populations (baseline and POD1, figure 3E), we observed that each population retained patterns of phenotypic gradients in their gene expression profiles, suggesting that the monocytes are on a spectrum of differentiation before and after surgery as opposed to being clearly defined postoperative monocytic cell subtypes. This is best exemplified by the observation that similar gradients of gene expression programs can be found in both baseline and POD1 states. To understand the differences in genes driving a global shift versus a gradient effect, we used non-negative matrix factorization (NMF) to learn distinct modules of coordinated gene expression.[25] This resulted in the identification of seven gene expression programs with variable activity in monocytes on Baseline and POD1 (NMF1-7; online supplemental figure S5). Some NMF programs (NMF1, NMF2 and NMF7) were mainly expressed in monocytes on POD1, while other NMF programs (NMF3, NMF4 and NMF6) had a similar expression at Baseline and POD1. Lastly, NMF5 was densely expressed in the CD16+monocyte populations (online supplemental figure S5).

We observed that M-MDSC gene signatures recently identified by scRNA-seq[26] were most expressed in the cells using NMF1 and 2 gene expression programs (figure 3G,H). Genes contributing to NMF1 and 2 included MDSC-related genes such as *S100a12, Hmgb2, Adam17, Hif1a, Ccr2, Il4r and Serpinb1*.[26–28] Notably, NMF4 activity was inversely correlated with this signature and driven by expression of genes involved in antigen presentation, including the HLA family genes (eg, *Hla.dra, Hla.drb1, Hla.dma, Hla.dpa1*) and *Tap1*, corroborating our GSEA results. Lastly, cells highly expressing NMF3 and 7 gene expression programs may be driven by individual patients, ARG12 and ARG19, respectively (online supplemental figures S4E and S5A). These NMF programs were also more expressed by POD1 cells and had high expression of genes related to MDSCs (*CEBPB, EIF4E, Trem1*, *Il1b*, *Tnf*, and *Ptgs2*).[29 30] Therefore, our NMF analysis showed that monocytes have varying levels of activity for each gene expression program, but that there was higher activity of NMF1, 2, 3, and 7 on POD1 with similarities to MDSC-related genes (figure 3I). These results implicate four different activity states of sx-MDSC, each contribute uniquely to the immunosuppressed period after surgery.

PI3K regulates sx-MDSCs suppressive machinery and is amenable to targeting

To identify pathways regulating the suppressive activity of MDSCs, we performed a series of compound screens using small molecules that affect major biological signaling pathways including PI3K/AKT, TGF-β, VEGF, NF-kB, COX, NOS, MMPs, and pathways governing apoptosis and autophagy (adMare Bioinnovations; figure 4A). In Screen #1 (online supplemental table S2), 147 compounds were incubated in MDSC:NK92 co-cultures for 1 hour at a final concentration of 1 µM and the compounds which prevent NK cell suppression by >50% were identified and used in Screen #2 (online supplemental table S3). In Screen #2, the compounds that resulted in the greatest reduction (online supplemental table S4) in MDSC suppression were compounds that targeted the PI3K pathway, such as LY294002 and AS-252424, suggesting a potential role for PI3K signaling in sx-MDSCs. Numerous reports have shown an important role for PI3K signaling in MDSCs.[31–33] Therefore, we investigated the role of PI3K in mediating the suppressive activity of sx-MDSC (figure 4B,C).

Although LY294002 can bind to multiple catalytic subunits of class I PI3K heterodimers, the p110-γ subunit is preferentially expressed in myeloid cells[31] and is known to regulate immunosuppressive profiles of tumor-associated myeloid cells.[31 33] To specifically target PI3K-γ, IPI-549 and TG100-115[31] were used in our co-culture assays. Similar to our findings with LY294002, both of these inhibitors improved NK cell cytotoxicity in our NK92:MDSC Suppression assay (figure 4D,E) as well as our healthy donor NK cell:MDSC suppression assay (figure 4F,G). These inhibitors also inhibited Akt phosphorylation in sx-MDSCs (online supplemental figure S6A). PI3K-γ specific inhibitors were more effective than LY294002 at reducing phospho-Akt in ex vivo whole blood experiments with and without IL-4 stimulation (online supplemental figure S6B). Notably, TG100-115 was also able to increase the MFI of HLA-DR when gated on sx-MDSCs in a dose-dependent manner, as has been reported by Kaneda *et al* (online supplemental figure S6B, n=1).[31]

Signaling through the PI3K pathway is increased following surgery

Given the results from the small molecule screen, we used PROGENy to infer relative differences in the signaling pathway activity of monocytic cells in our

scRNA-seq. On POD1, there was significant upregulation in several signaling pathways: VEGF, PI3K, hypoxia, MAPK, androgen, nuclear factor-κB (NF-κB), and TNF-α. Conversely, there was a decrease in JAK-STAT and WNT signaling, while TGF-β, p53 and Trail signaling did not differ significantly after surgery (figure 5A). Importantly, PI3K signaling pathway activity was upregulated in all patients (figure 5B). Consistent with our functional data, PI3K-regulated transcripts were significantly altered in monocytes after surgery. To determine which NMF program in our monocyte population was associated with elevated PI3K activity, we queried our scRNA-seq against publicly available gene sets of PI3K-regulated genes.[34] The NMF programs that had the highest correlation with PI3K-regulated genes were NMF1 (r=0.22) and 2 (r=0.32), suggesting that these putative sx-MDSC gene programs are also associated with elevated PI3K activity. Therefore, the PI3K signaling pathway is transcriptionally elevated in sx-MDSCs.

Next, we investigated if these transcriptional changes in PI3K were associated with alteration in PI3K signaling. Since PI3K signaling leads to AKT phosphorylation, specifically at residue T308, monitoring the phosphorylation status of this "master regulator" could be a surrogate for PI3K activity (figure 5C).[31] Phosphorylation of AKT at the T308 residue was significantly greater in POD1 M-MDSCs than baseline, and there were no changes in S473 phosphorylation. PI3K-γ inhibitor treatment (IPI-549 and TG100-115) led to a dose-dependent reduction in AKT phosphorylation, indicating a reduction in PI3K-γ signaling comparable to LY294002. Moreover, these inhibitors reduced sx-MDSC-mediated suppression of NK cell cytotoxicity and did not affect cytotoxicity in the absence of sx-MDSCs (figure 5D). However, we note that these inhibitors had a negative effect on cytotoxicity at higher concentrations when plated with NK92-MI alone (online supplemental figure S7).

Finally, we investigated the role of PI3K-γ in mediating the expression of immune effector mRNA transcripts such as anti-inflammatory transcripts, *Arg1*, *Il10*, *Tgfb* as well as pro-inflammatory transcripts, *Il1b*, *Il12b*, *Tnfa, Il6, and Ccl2* in MDSCs isolated from Baseline and POD1 (figure 5E). Surgical stress caused a significant decrease in all pro-inflammatory transcripts, *Il1b*, *Il12b, Il6* and *Ccl2*, while anti-inflammatory *Arg1* was upregulated. PI3K-γ blockade with IPI-549 treatment in POD1 sx-MDSCs prevented the surgery-induced reduction of pro-inflammatory transcripts *Il1b*, *Il6* and *Il12b*; however, it did not rescue *Ccl2* mRNA expression.

PI3K inhibitors inhibit sx-MDSCs in preclinical murine models of surgical stress

In a preclinical model, we have shown that murine PMN-MDSCs ($Gr1^+CD11b^+Ly6G^+$) and M-MDSCs

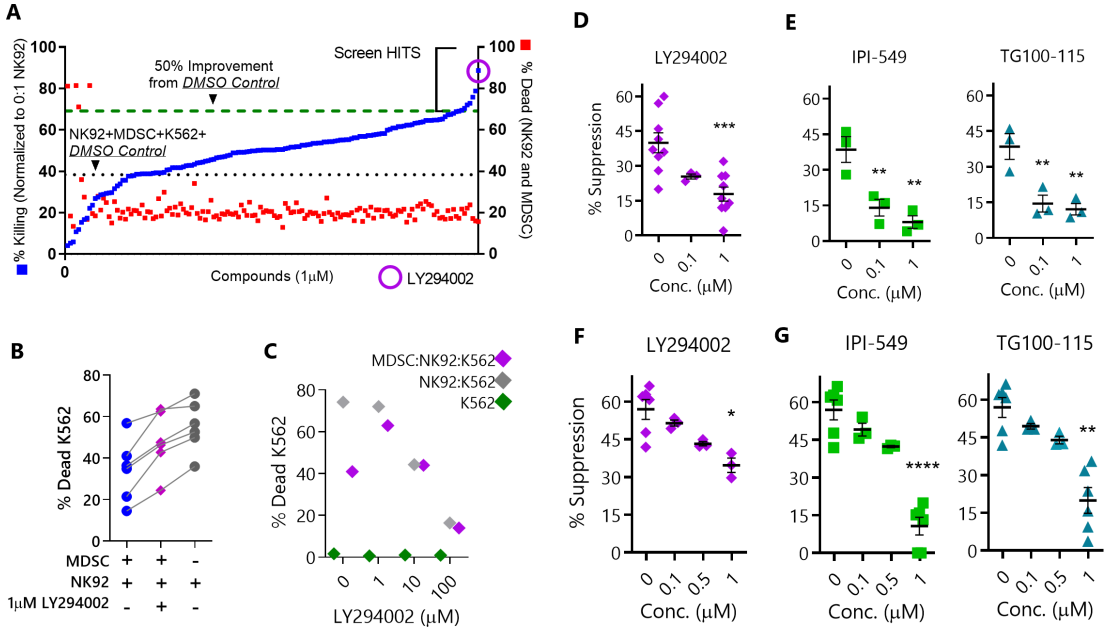

Figure 4 PI3K inhibitors reverse the suppressive effects of sx-MDSCs on NK cells. (A) A library of 147 small molecules covering the major cellular signaling pathways was screened (n=4 experiments) at 1 μM in the MDSC-NK suppression assay. Compounds that improved NK cell cytotoxicity (blue, left y-axis) by >50% from DMSO control (black dotted line), without impacting NK cell viability (red, right y-axis), were considered hits. LY294002 (purple circle) improved cytotoxicity in all screens and was the top hit in 3/4 screens. (B) LY294002 improves NKC (n=6). (C) Dose response of LY294002 and the effect on NKC and K562 viability. (D) pan-PI3K and (E) PI3K-γ specific inhibitors (IPI-549, TG100-115) in NK92—MDSC suppression assays. (F) pan-PI3K and (G) PI3K-γ specific inhibitors (IPI-549, TG100-115) in MDSC suppression assays with primary healthy donor NK cells. Statistical analysis used one-way ANOVA with Dunnett's multiple comparisons test. ***p<0.0001. ANOVA, analysis of variance; DMSO, dimethyl sulfoxide; MDSC, myeloid-derived suppressor cell; NK, natural killer; sx-MDSC, surgery-induced MDSC.

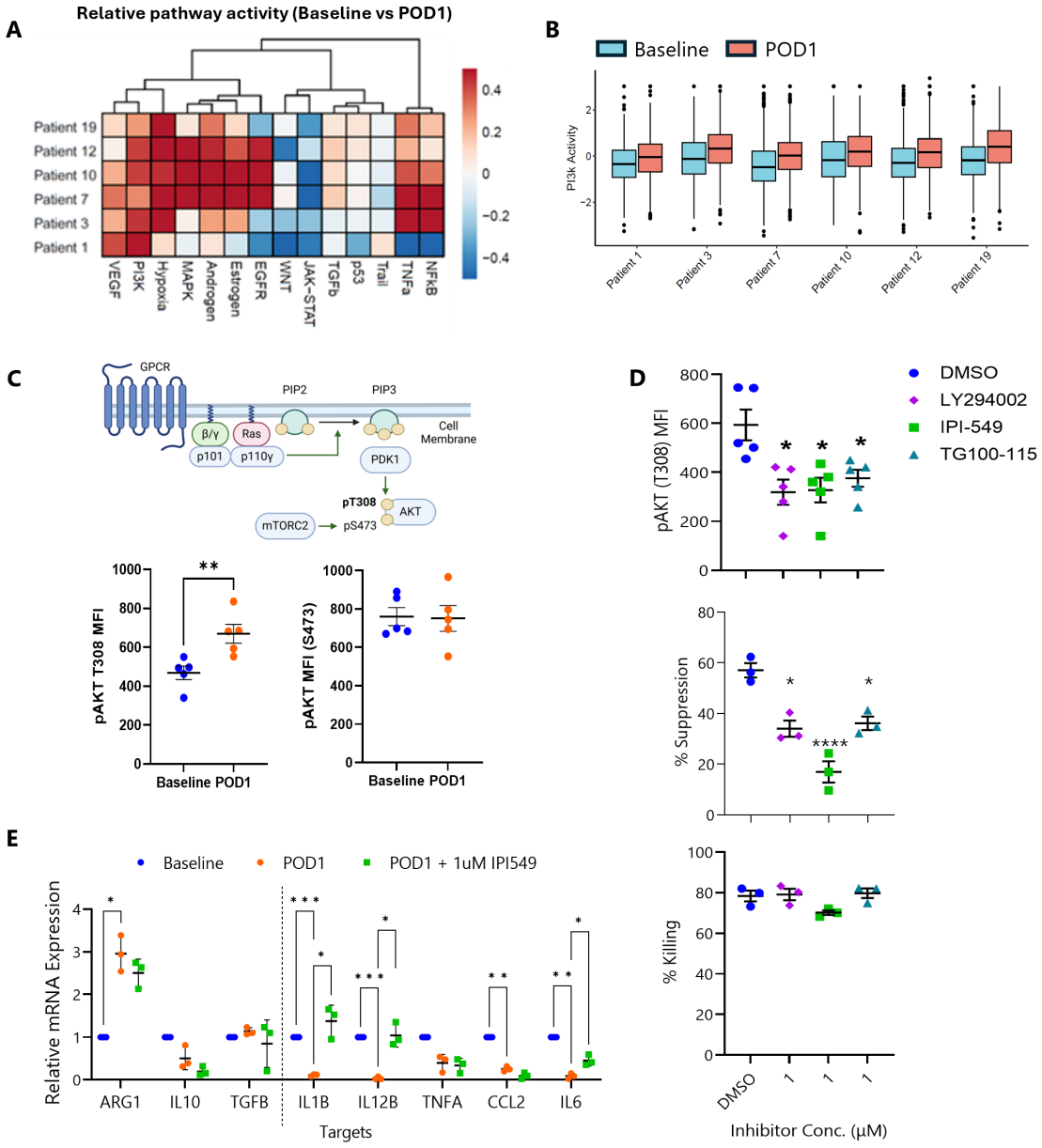

Figure 5 PI3K pathway activation in postoperative MDSCs and functional impact of PI3K inhibition. (A) Cohort of differentially expressed genes from baseline versus POD1 MDSCs. (B) Box plot inference of PI3K pathway activity in baseline versus POD1 MDSCs. (C) Pathway diagram of PI3K signaling and Akt phosphorylation. Phosphorylation status of AKT at the T308 (left) and S473 residue (right) (n=5). (D) Effect of PI3K inhibitors on pAKT (T308) MFI (top), MDSC-NK suppression (middle), and NKC (bottom). (E) Effect of IPI-549 on POD1 expression of anti-inflammatory versus pro-inflammatory mRNA transcripts, normalized to baseline. Statistical analysis used Wilcoxon matched pairs signed-rank tests and one-way ANOVA with Dunnett's multiple comparisons test (vs DMSO control). ****p>0.0001. ANOVA, analysis of variance; ARG1, arginase-1; CCL, CC chemokine ligand; DMSO, dimethyl sulfoxide; IL, interleukin; MDSC, myeloid-derived suppressor cell; mRNA, messenger RNA; MFI, mean fluorescence intensity; NK, natural killer; POD1, postoperative day 1; TGF, transforming growth factor; TNF, tumor necrosis factor.

(Gr1^{dim}CD11b^{+}Ly6C^{+}) increase after surgery.[12] In the present study, we assessed whether PI3K inhibitors can be used to reduce the suppressive effects of sx-MDSCs in mice. PI3K-γ inhibitors resulted in a dose-dependent reduction in AKT phosphorylation in ex vivo murine sx-M-MDSCs and sx-PMN-MDSCs (figure 6A). Murine sx-MDSCs stimulated with IL-4 had increased phosphorylation of AKT and served as a positive control. Next, we investigated whether surgical stress alone influenced PI3K-γ pathway activation in murine sx-MDSCs. We observed a significant increase in pAKT MFI in both sx-MDSC subsets on POD1 compared with no surgery controls, which was significantly reduced when mice were treated with perioperative TG100-115 (6 mg/kg) or IPI-549 (30 mg/kg), in M-MDSCs but not PMN-MDSCs (figure 6B).

To assess whether PI3K inhibitors can prevent sx-MDSC-mediated suppression of NK cell cytotoxicity,

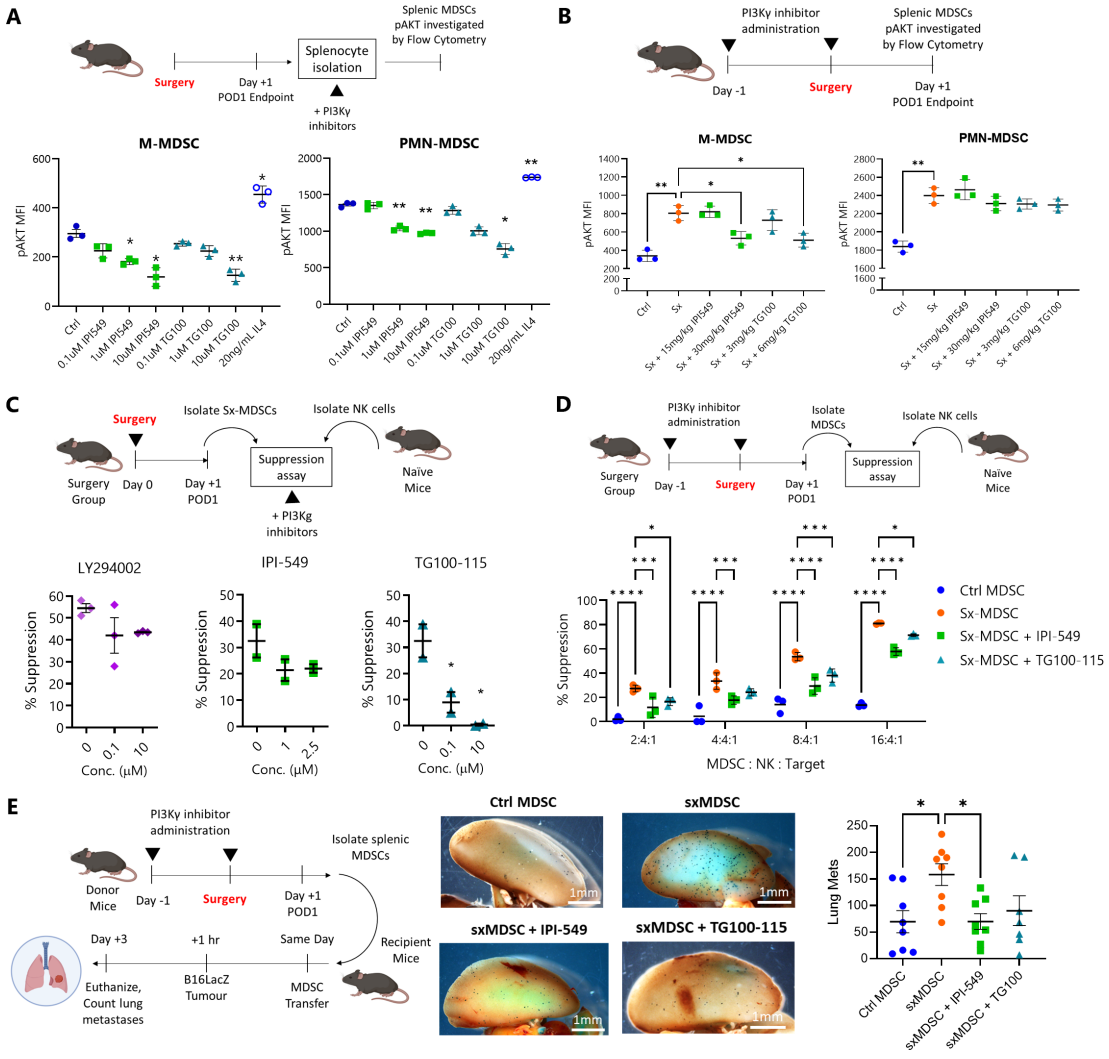

Figure 6 Blockade of PI3Kγ signaling in sx-MDSCs reduces NK cell suppression and metastatic disease in mouse models of surgical stress. (A) Ex vivo effect of PI3K inhibitors on pAKT (T308) phosphorylation in splenic MDSCs from C57Bl/6 mice (n=4). (B) Effect of preoperative in vivo administration of PI3K inhibitors on pAKT (T308) phosphorylation measured on POD1 in splenic MDSCs (n=4). (C) Ex vivo effect of PI3K inhibitors on MDSC-NK %suppression (n=3). (D) Effect of preoperative in vivo administration of PI3K-γ inhibitors on sx-MDSC suppressive capacity. (E) Adoptive transfer of representative images of lungs is shown. One-way ANOVA with Holm-Sidak or two-way ANOVA with Dunnett's multiple comparisons tests were performed. ****p<0.0001. ANOVA, analysis of variance; M-MDSC, monocytic-MDSC; MDSC, myeloid-derived suppressor cell; MFI, mean fluorescence intensity; NK, natural killer; sx-MDSC, surgery-induced MDSC, PMN-MDSC, polymorphonuclear-MDSC; POD1, postoperative day 1.

we first tried an ex vivo suppression assay, where MDSCs ($Gr1^+$) cells from surgically stressed mice were co-cultured with naïve NK cells from control mice, in the presence of PI3K inhibitors (figure 6C). We observed a dose-dependent reduction of NK cell cytotoxicity suppression in ex vivo co-cultures treated with the PI3K inhibitors. Next, we investigated the effect of treating mice perioperatively with TG100-115 or IPI-549. MDSCs from these perioperatively treated mice were then isolated and co-cultured with NK cells from naïve mice (figure 6D) in our suppression assay. The sx-MDSCs isolated from mice perioperatively treated with PI3K inhibitors were significantly less suppressive than sx-MDSCs from control mice. However, we observed that systemic perioperative PI3K-γ inhibitor treatment also had a negative effect on NK cell function and led to increased tumor metastases, as well as reduced ex vivo NK cell cytotoxicity against Yac-1 targets compared with mice that only received surgery (online supplemental figure S8). This effect may be due to off-target effects of PI3K inhibitors on NK cells.[35 36]

Therefore, in order to assess the effects of PI3K-γ inhibition on sx-MDSCs in isolation, we performed an adoptive transfer of systemically treated sx-MDSCs into naive mice, which were then inoculated with B16F10lacZ tumor cells so that we could measure the resulting lung tumor burden after 3 days (figure 6E). The adoptive transfer of sx-MDSCs caused a significant increase in lung metastases

compared with no-surgery controls, recapitulating the premetastatic effect of sx-MDSCs, while the adoptive transfer of sx-MDSCs from mice treated with IPI-549 developed significantly fewer lung metastases.

DISCUSSION

The earliest report of NK cell suppression by a surgery-induced suppressive monocytic cell population was in 1982 by Uchida and colleagues.[37] Decades later, as our understanding increased, it is likely that Uchida *et al* was investigating sx-MDSCs. Only recently has the umbrella term "MDSC" become an accepted nomenclature for the heterogeneous population of immunoregulatory myeloid cells.[5] Numerous context-dependent identifiers have been used to further categorize MDSCs to bring greater clarity and accuracy to the field. This is because factors such as tissue localization, disease state, including cancer subtype and inflammatory conditions, can all contribute to differing MDSC subtypes.[16]

MDSCs have been best characterized in patients with cancer as immature myeloid cells that directly suppress immune effector cells in the tumor microenvironment.[33 38] "Surgery-induced" or "trauma-induced" has been used by our group[13] and others[6 39] as a prefix for MDSCs that arise from sterile (non-microbial), surgical inflammatory conditions (ie, inflammatory response to host-derived DAMPs).[40] Here, we wanted to determine the contribution of sx-MDSCs, in the inflammatory context of cancer. To that end, we assessed the changes in MDSC populations from a diverse cohort of cancer surgery patients differing in their primary cancer and surgical procedures (table 1). This allowed us to assess the universal effect of surgery-induced inflammation on postoperative MDSCs. Despite varying starting M-MDSC levels at baseline, the median fold change was higher in M-MDSCs than PMN-MDSCs across all cancer types, apart from lung cancer surgery patients (online supplemental figure S2). In studies where there was a specific cancer type, similar results were reported. Wang *et al*[6] observed that the M-MDSCs were the main MDSC subtype after surgery in a cohort of lung cancer surgery patients. Gao *et al*[41] reported that high systemic inflammation following surgery in patients with hepatocellular carcinoma was correlated with a greater expansion of M-MDSCs that was also correlated with a shorter time to recurrence and shorter overall survival. Grauers Wiktorin *et al*[39] found expansion of M-MDSCs in pancreatic cancer surgery patients, linking their presence with a reduced overall survival following surgery as well. In the latter study, programmed death-ligand 1 (PD-L1) cell surface expression increased modestly postoperatively on POD3 to 5 but not on POD1, similar to our results. They also measured a significant increase in reactive oxygen species (ROS) on POD1, which we have previously seen in murine sx-MDSC[13] but did not measure in human sx-MDSCs in this study.

When comparing PMN-MDSCs and M-MDSCs, PMN-MDSCs had a higher scatter profile compared with M-MDSCs, in addition to greater expression of Arg1, CD124, and Lox1. Lox1 was recently described as a distinguishing biomarker for PMN-MDSCs[17] and in our study, Lox1 had a higher postoperative MFI in both sx-MDSC subtypes (figure 1E). However, although M-MDSCs also expressed Arg1 and CD124, the MFI of these markers did not increase after surgery in M-MDSCs. M-MDSCs made up the bulk of the sx-MDSC population and had more suppressive capacity when they were separately enriched for, compared with PMN-MDSCs (figure 3E).

Single-cell mass cytometry profiling in patients undergoing hip arthroplasty surgery showed the greatest immune cell perturbations occurred in $CD14^+$ monocytes, which resembled the phenotype of immunosuppressive MDSCs.[24] Similarly, our study showed the most striking differences in transcription were within the monocytic compartment after surgery. We observed that gradients of gene expression patterns were present at baseline and POD1, suggesting that sx-MDSCs are on a continuum of differentiation as opposed to distinct terminal stages of differentiation or maturity (figure 3). Querying our data set against a publicly available gene set of M-MDSCs,[26] we saw that the gene expression profile overlapped with NMF1 and NMF2. The genes that drive these expression programs in our data set were increased DAMPs (eg, *Hmgb2, S100a8/9/12*) and chemokines (eg, *Ccr2*) in addition to decreased HLA gene expression (figure 3). Interestingly, NMF4 had the inverse gene expression program of NMF 1 and 2, with very high expression of HLA-DR. Since NMF4 activity was mainly expressed in monocytes at baseline (online supplemental figure S5B), this supports the hypothesis that after surgery, emergency myelopoiesis results in an expansion of immature myeloid cells that gain a suppressive phenotype because of the postoperative inflammatory context. A limitation of our scRNA-seq experiments is that we are unable to make firm inferences about PMN-MDSCs due to the negative effect of cryopreservation on PBMC viability and recovery of PMN-MDSCs.[15] Furthermore, specific genes that define MDSC suppressive mechanisms, Arg1 in particular, are untraceable on freeze-thawing.[42]

The small molecule screen helped to identify pathways regulating sx-MDSC suppression, an included compounds that targeted TGF-β, VEGF, Raf/MAPK, and NF-κB/TNF-α pathways which were transcriptionally upregulated following surgery by scRNA-seq. The compounds GW5074 and Bay11-0785, which inhibit Raf/MAPK and NF-κB/TNF-α, respectively, were among the top compounds that inhibited sx-MDSCs (online supplemental table S4). The PI3K-γ pathway was pursued because a pan-PI3K inhibitor was the top hit in our screens (figure 4A) and was activated in myeloid cells postoperatively based on scRNA-seq (figure 5B). Furthermore, the PI3K-γ isoform has been reported as the regulator for macrophage polarization and immunoregulatory programs.[31 32] van Wigcheren *et al*[43] demonstrated that PI3K-γ inhibition reversed the

immature phenotype of MDSCs, shown by increased HLA-DR expression and decreased expression of immunosuppressive markers, MerTK and ROS. De Henau *et al*[32] demonstrated that selective PI3K-γ isoform inhibition, with IPI-549, reduced the suppressive activity of tumor-associated MDSCs. In addition, IPI-549 overcame resistance to anti-programmed cell death protein-1 as well as anti-cytotoxic T-lymphocyte associated protein 4 checkpoint blockade therapy, leading to enhanced antitumor immunity and tumor regression in mouse models of cancer. Davis *et al*[19] reported that inhibiting p110γ enhanced the efficacy of anti-PD-L1 immunotherapy in head and neck squamous cell carcinoma by modulating cytotoxic immune activity against tumors and inhibiting MDSC activity.

We confirmed upregulation of PI3K activity by demonstrating increased phosphorylation of pAKT (T308) in both humans (figure 5C) and in our murine model (figure 6B), which was reversed with PI3K-γ blockade. Therefore, at the signaling level, PI3K-γ is activated in postoperative M-MDSCs and is amenable to therapeutic blockade. We focused on the blockade of the p110-γ catalytic subunit of PI3K because it is the isoform predominantly expressed by myeloid cells and the PI3K-γ specific inhibitors, IPI-549 and TG100-115, were more potent in inhibiting sx-MDSCs in vitro (figure 4D–G; figure 6C) and in vivo (figure 6D). Similar to prior studies,[19 31 32] we found that sx-MDSCs exhibit a predominantly anti-inflammatory phenotype, characterized by upregulation of Arg1 and downregulation of pro-inflammatory markers such as IL-6, IL12B, CCL2, and IL1B. Although PI3K-γ inhibition in sx-MDSCs did not prevent the upregulation of Arg1 expression, it did result in a marked increase of IL-6, IL12B, and IL1B (figure 6E). This further supports the role of PI3K-γ targeting to prevent or reverse postoperative immune suppression.

This study is the first to demonstrate the therapeutic potential of perioperative PI3K-γ inhibitors in preventing postoperative immune suppression and metastatic recurrence. While systemic delivery of PI3K inhibitors reduced MDSC suppression after surgery, these inhibitors also had negative effects on NK cell activity and resulted in increased postoperative tumor burden (online supplemental figure S8). PI3K-γ plays a critical role in NK cell migration, development, and effector functions.[35] It is also required for cytotoxic activity, NK cell-target cell interaction and receptor-induced IFN-γ production.[35] In addition to its effects on NK cells, systemic inhibition of PI3K signaling can also impair T-cell function, affecting both effector and regulatory subsets, which may have unintended perioperative consequences.[44] Therefore, targeting these potent PI3K inhibitors specifically to sx-MDSCs is absolutely required to limit off-target effects. Our experiments confirm this because the adoptive transfer of sx-MDSC from mice treated with PI3K-γ inhibitors did not recapitulate the postoperative tumor burden as seen in the no-treatment control group (figure 6E).

A potential therapeutic strategy to selectively target sx-MDSCs is the use of antibody-drug conjugates (ADC), which have conventionally been explored to deliver a cytotoxic payload to tumor cells. In this context, an ADC carrying a PI3K-γ inhibitor could be targeted to unique cell surface proteins on sx-MDSCs, such as CD33/CD14 or Lox1, which is upregulated on sx-MDSCs. In addition, although PI3K-γ has shown significant efficacy in preclinical models, little is known about its clinical safety and efficacy. Clinical trials exploring pan-PI3K inhibitors[45] have demonstrated toxicities such as hyperglycemia, cutaneous reactions, diarrhea/colitis, and pneumonitis.[45] Therefore, targeted sx-MDSC-specific approaches may also mitigate toxicities associated with systemic PI3K-γ blockade.

In summary, the perioperative period is a dynamic landscape occupied by immunosuppressive monocytic sx-MDSCs which have heterogeneous transcriptional profiles. Scoring gene sets from MDSCs generated in different inflammatory settings will help identify the context-specific attributes of MDSCs and bring greater clarity and accuracy to the field. Currently, no perioperative therapy is approved to target sx-MDSCs, but we have shown preliminary evidence that sx-MDSCs rely on PI3K signaling for their suppressive activity. Indeed, PI3K controls the transcriptional regulation of the immunosuppressive programming in sx-MDSCs; however, given the critical role of PI3K signaling in antitumor immunity, particularly in NK cell function, strategies to specifically target sx-MDSCs need to be explored. Moreover, given the rapid activation of sx-MDSCs soon after surgery with resultant NK cell dysfunction, preoperative PI3K blockade in sx-MDSCs may pre-emptively prevent this immunosuppressive phenotype from arising. One may question how a relatively short period of profound immune suppression could lead to the discovery of metastases months to years later, but recent studies have clearly demonstrated that the detection of circulating tumor DNA within 3–6 weeks after surgical resection for cancer is highly predictive of recurrence in colorectal,[46] lung,[47] and breast cancer.[48] Supporting a functional immune system to clear microscopic disease in the early postoperative period is a highly promising strategy to reduce recurrences, providing clinical rationale for a therapeutic strategy that directly targets the underlying mechanism behind postoperative immune suppression.

MATERIALS AND METHODS

Study design

To characterize sx-MDSCs, we used PBMCs or "ACK" (ammonium-chloride-potassium) lysed whole blood from patients (n=55) enrolled under the Perioperative Human Blood and Tissue Specimen Collection Program. Inclusion and exclusion criteria were determined prospectively. Consenting participants over the age of 18 undergoing a surgical procedure for their cancer treatment were included in the study. Patients who were previously

treated with chemotherapy, radiation, or immunotherapy and received blood transfusions during surgery were excluded from the study. The patient samples collected under this study protocol were used in all experiments, excluding the scRNA-seq (table 1).

To control for inter-assay variability, antibodies were titrated and stained following a standard flow cytometry staining protocol using previously determined gates and voltages. Voltages for excitation/emission spectra were routinely assessed to ensure that MFI values could be compared between baseline and POD1, and across different patient samples on different days of experimentation. Lastly, a core panel of antibodies was used to phenotype MDSCs by flow cytometry, with the capacity to include additional exploratory markers. Patient samples were used in multiple experiments to ensure the ethical and efficient use of patient materials.

To explore the transcriptional changes occurring after surgery in sx-MDSCs, we performed scRNA-seq from six cryopreserved PBMCs from abdominal cancer surgery patients (online supplemental table 1) enrolled in the PERIOP-02 clinical trial (NCT02987296; OHSN-REB# 20160732–01 hour). These patients were instructed to take a supplement enriched in arginine (n=3) or an isocaloric/isonitrogenous control supplement (n=3) three times a day for 5 days as part of the trial.[49] To account for the potential impact of the differences in treatments, we performed a separate analysis comparing the transcriptional changes between groups and did not find any effect attributable to the supplement given (online supplemental figure S4). Furthermore, the patient samples selected for the scRNA-seq had similar demographic, procedural and surgical outcome data (online supplemental table 1). Therefore, we combined all six patients in our final analysis to increase our statistical power.

Human blood sample collection and processing

Patient (baseline and POD1) and healthy volunteer peripheral blood samples (20–40 mL) were drawn at The Ottawa Hospital with informed consent under the following clinical protocols: (1) OHSN-REB# 20160732–01 hour and (2) OHSN-REB# 2011884–01 hour. Blood was drawn into BD Vacutainer Sodium-Heparin coated tubes and processed within 2 hours by Ficoll density centrifugation (GE HealthCare #17-1440-03).

Antibodies for phenotyping by flow cytometry

The panel of MDSC markers was chosen based on published guidelines to harmonize human MDSC reporting led by the Association for Cancer Immunotherapy, Cancer Immunoguiding Program[15]—with slight modifications. Freshly isolated PBMCs were first labeled with a fixable viability stain (BV510; BD #564406) in phosphate-buffered saline (PBS) at room temperature for 10 min. Next, an extracellular MDSC antibody mastermix was added to the PBMCs and simultaneously stained with the viability dye for an additional 20 min at 4°C. The antibodies in the MDSC mastermix were used at individually titrated dilutions and included: CD33 clone P67.6 (Pe-Cy7, BioLegend #366617), CD14 clone MθP9 (APC-Cy7, BD #561709), CD11b clone ICRF44 (AF700, Novus #FAB1699N), HLA-DR clone L243 (APC, BioLegend #307609), CD15 clone MMA (efluor450, eBioscience #48-0158-41), CD124 clone 25463 (PE, R&D systems #FAB230P-025), and lineage markers CD3 clone UCHT1 (FITC, BioLegend #300440), CD56 clone NCAM16.2 (FITC, BD Biosciences #340410) and CD19 clone HIB19 (FITC, BioLegend #302205).[15] Exploratory extracellular markers included LOX-1 clone 15C4 (PE, BioLegend #358603), VISTA clone 730804 (AF700, R&D systems #FAB71261N), and PD-L1 clone MIH1 (PE, eBioscience #12-5983-42). Following viability and extracellular staining, PBMCs were washed and resuspended in 1% paraformaldehyde (PFA) and acquired by flow cytometry within 48 hours. For intracellular staining, the BD Cytofix/Cytoperm kit (BD #554714) was used after viability and extracellular staining and cells were incubated in Perm/Wash buffer with Arg1 (APC, R&D systems #IC5868A) for 30 min at 4°C. Samples were acquired on the BD Fortessa LSRII and analyzed with FlowJo V.10.

Cell lines and isolation of sx-MDSC subsets and high-density neutrophils

PBMCs from whole blood taken on POD1 were processed through two workflows to isolate M-MDSCs ($CD33^+CD14^+CD15^-$) and PMN-MDSCs ($CD33^{dim}CD14^{-/dim}CD15^+$) (online supplemental figure S3). For M-MDSC isolation, $CD33^+$ cells were first separated using $CD33^+$ microbeads (Miltenyi #130-045-501) via immunomagnetic bead separation. Similarly, PMN-MDSCs were isolated by first obtaining $CD15^+$ cells using $CD15^+$ microbeads (Miltenyi #130-046-601). Both starting populations were then stained with a simplified immunophenotyping panel containing: CD33 clone P67.6 (Pe-Cy7, BioLegend #366617), CD14 clone MθP9 (APC-Cy7, BD #561709), CD15 clone W6D3 (PE, BD Biosciences #562371), L/D (APC, Thermo Scientific #L34975). The stained $CD33^+$ and $CD15^+$ cells underwent fluorescence-activated cell sorting using the Sony MA900 Multi-Application Cell Sorter to isolate live M-MDSCs ($CD33^+CD14^+CD15^-$) and PMN-MDSCs ($CD33^{dim}CD14^{-/dim}CD15^+$), respectively.

HDNs were isolated via double density centrifugation by overlaying 6 mL whole blood on top of 3 mL Histopaque 1077 (Sigma-Aldrich #10771), which was first overlaid on top of 3 mL Histopaque 1119 (Sigma-Aldrich #11191). After centrifugation at 700×g for 30 min with brakes off, the PBMCs were collected from the upper interface, followed by HDN collection from the bottom interface.

MDSC:NK92 suppression assay

K562 and NK92-MI cell lines were purchased from American Type Culture Collection (ATCC) and maintained in Roswell Park Memorial Institute (RPMI) medium +10% fetal bovine serum (FBS) termed "complete RPMI" (cRPMI). MDSC-mediated NK cell suppression was measured by isolating MDSCs from surgery patients on

POD1 and incubating them in cRPMI at increasing ratios with the IL-2 independent NK cell line, NK92-MI for 20 hours at 37°C. Following incubation, K562 target cells labeled with Cell Proliferation Dye eFluor 450 (CP450, eBioscience #65-0842-90) were added to the MDSC:NK co-cultures for 4 hours. NK cell cytotoxicity was then measured by adding ethidium homodimer (EtHD, Invitrogen #E1169) to each well just prior to acquiring the samples by flow cytometry. NK cell cytotoxicity was reported as %dead K562 (EtHD+ CP450+). To calculate %MDSC suppression, we used the following equation:

$$\left(1 - \frac{(\%\,dead\ K562_{MDSC:NK})}{(\%\,dead\ K562_{NK\ alone})}\right) \times 100\% = \%\,MDSC\ suppression$$

Primary healthy donor NK cell:MDSC suppression assay

NK cells were isolated from whole blood using the autoMACS Pro Separator and StraightFrom Whole Blood CD56 MicroBeads (Miltenyi Biotec, #130-090-875), following the manufacturer's protocol. Isolated CD56+NK cells were resuspended in cRPMI and plated in a 96 V-bottom well plate. Sx-MDSCs isolated from PBMCs of surgery patients on POD1 were plated in increasing ratios with or without PI3K inhibitors and incubated for 24 hours with 100 U/mL of IL-2. After the incubation, CP450 labeled K562 target cells were plated and NK cell cytotoxicity was quantified 4 hours after by flow cytometry (as described above).

Giemsa-Wright staining and microscopy

Freshly isolated PBMCs were washed two times in MilliQ H_2O and resuspended in 20 µL of MilliQ H_2O. 5–10 µL of PBMCs were pipetted onto a glass slide and gently smeared with the long edge of a 20 µL pipette tip. Slides were fixed with 100% MeOH and air dried for 2 min. At this point, 0.5–1 mL of undiluted stock Giemsa-Wright stain (Sigma #WG80-2.5L) was pipetted onto the slides and left for 2 min to stain. Afterward, excess Giemsa-Wright stain was poured off and the slides were submerged into a diluted Giemsa-Wright stain (1:20, stain:MilliQ H_2O) for 5 min. Slides were then gently submerged into MilliQ H_2O to rinse and left to air dry. Slides were viewed and imaged the same day (Nikon Te2000e, The Ottawa Hospital Research Institute).

Single-cell RNA sequencing library preparation and sequencing

Cryopreserved and matched baseline/POD1 PBMC patient samples (n=6) were used for scRNA-seq on the 10x Genomics Chromium Single Cell 3' platform (Stem-Core Laboratories, the Ottawa Hospital Research Institute). Baseline and POD1 samples were multiplexed into separate pools using MULTI-seq before being processed on two lanes of the Chromium platform superloaded to target a 20,000 cell yield per lane. Briefly, each sample was labeled for 10 min with 200 nM of a unique DNA barcode hybridized to complementary lipid-modified DNA enabling anchoring to the cells' plasma membrane. Each sample was washed two times with PBS + 1% bovine serum albumin (BSA) prior to pooling. Gene expression libraries were prepared following the standard 10x Genomics protocol, and separate MULTI-seq barcode libraries were isolated by size selection and PCR amplified as described by McGinnis *et al* (https://github.com/chris-mcginnis-ucsf/MULTI-seq). Libraries were sequenced using NextSeq 500 (Illumina) high-output 75-cycle runs. Gene expression libraries were sequenced to a depth of approximately 20,000 reads/cell and MULTI-seq barcode libraries were sequenced to a depth of approximately 1000 reads per cell, which is sufficient for sample annotation.

scRNA-seq data processing and pipeline

Following sequencing, FASTQ files were generated using the Cell Ranger mkfastq tool (10x Genomics). Gene expression libraries were processed using the Cell Ranger count function, aligning to the human transcriptome (GRCh38) with default parameters other than explicitly setting –expect-cells 20,000. MULTI-seq barcode fastq files were processed using the deMULTIplex tool developed for MULTI-seq (https://github.com/chris-mcginnis-ucsf/MULTI-seq), providing a sample annotation for each cell barcode.

Gene expression libraries were imported into R and processed with Seurat.[50] Cells containing high proportions of mitochondrial reads were first removed before splitting the data into separate 12 Seurat objects representing each unique sample. Each sample was normalized using SCTransform prior to integration using Seurat's SCTransform integration pipeline.[50 51] The integrated data was then processed with principal component analysis (PCA) and clustered using the Louvain algorithm (resolution=0.15) on a neighbor graph derived from the first 30 principal components. Deriving cluster identities based on the integrated data ensured that clusters were not associated with variability of each patient or experimental groupings (ie, baseline/POD1). Each cluster was annotated based on expression of canonical markers of PBMC populations.

Following clustering, unintegrated data was re-processed using SCTransform, PCA, and uniform manifold approximation and projection (UMAP) embedding, providing a low-dimensional representation of the data capturing biological variability of interest while retaining cluster annotations that represent the underlying cell type. We then used the R tool muscat to perform differential state analysis between POD1 and baseline samples within each cluster.[20]

Signaling pathway activity inference

The R package PROGENy was used to infer the activity of 14 signaling pathways in each cell of the data.[52] PROGENy derives activity scores using a regression model trained on data from transcriptional profiles from hundreds of signaling perturbation experiments. After inferring activity scores, we tested for pathways with differential activity between cells from POD1 and baseline samples using a simple linear model.

Gene Set Enrichment Analysis

The R package fgsea was used to perform GSEA on genes ranked by their average log fold change from the differential state analysis for individual cell types (http://bioconductor.org/packages/fgsea/). Lists of all GO terms, KEGG pathways, Reactome pathways, and Hallmark gene sets were acquired from the Molecular Signatures Database (MSigDB).[21 22] All gene sets presented in the manuscript are significantly enriched (adjusted p value<0.05) and normalized enrichment scores are presented.

Identification of coordinated gene expression programs

To identify coordinated gene expression programs that represent continuous phenotypic gradients, we applied consensus NMF to normalized gene expression counts for the top 2,000 variable genes (based on variance computed by SCTransform), as implemented in the NMF tool described by Kotliar *et al*.[25] To identify the appropriate number of programs to identify (factors; k), we used NMF to perform 100 iterations of NMF for each k from 2 to 10. k=7 provided stable factorizations with low error and was used for downstream analysis (online supplemental figure S5). Consensus NMF then identifies a consensus factorization based on the 100 iterations for a given k. The "cell usage" and coefficient matrices resulting from the factorization were then imported into R. As a gene's coefficient is ultimately dependent on its average expression level, we Z-score-transformed each gene's coefficients across the NMF programs and ranked genes by their Z-score value for each NMF program. To gain insight into which biological phenotypes may be associated with each NMF program, we calculated correlated cells' NMF program usages with gene set scores from MSigDB and publications of interest.

Gene set scoring and autocorrelation

Gene set scoring was performed using Vision.[53] Similar to complementary tools, Vision computes a score for query gene sets based on the average expression of each gene relative to background control gene sets. Vision also calculates an autocorrelation score (1-Geary's C) for each gene set, providing insight into whether gene set activity represents coordinated variation in latent space (k-nearest neighbors, kNN, graph from 50-dimensional PCA space) or if the scores are randomly distributed.

Small molecule screen for MDSC antagonists

Our MDSC antagonist screens were separated into two screens (Screen #1 and Screen #2) which were each performed two times. Screen #1 included 147 unique small molecule compounds plated in singlets at 1 µM (online supplemental table 2). Screen #1 was created in collaboration with adMare Bioinnovations (British Columbia, Canada). The library was plated in 96 V-bottom plates and shipped on dry ice via priority courier to the OHRI where the suppression assays were done immediately on receiving the compounds. Each plate contained their own dimethyl sulfoxide (DMSO) and media only wells in which control samples were plated. Sx-MDSCs were isolated from cancer surgery patients on POD1 and plated at a 4:1 sx-MDSC:NK92 cell ratio±drug compounds for 24 hours prior to adding CP450-labeled K562 cells. Compounds which led to the greatest improvement in NK cell cytotoxicity (hits) from Screen #1 informed the creation of Screen #2 which included a refined list of only 40 compounds, plated in duplicates, at 1 µM and 10 µM (online supplemental table 3). Drugs were plated in a randomized order and kept blinded from experimenters until after completing the analysis.

Phospho-signaling assay

For in vitro phospho-AKT staining, PBMCs (humans) or splenocytes (mouse) were incubated for 3 hours with or without PI3K-γ inhibitor treatment in cRPMI at 37°C in a 5% CO_2 chamber. During the last 15 min of incubation, MDSCs were stained with an antibody panel for immunophenotyping. Splenocytes underwent a simultaneous Lyse/Fix step using Lyse/Fix buffer (BD Biosciences # 558049) while PBMCs were fixed with fixation buffer (BD Biosciences #554655), and both were incubated for 10 min at 37°C. Samples were then permeabilized using Perm buffer III (BD Biosciences #558050), according to the manufacturer's protocol. Cells were washed two times with flow buffer and then stained with AKT pT308 Clone D25E6 (PE, Cell Signaling Technology #13038S) and AKT pS473 Clone M89-61 (AF647, BD Biosciences #561670) for 1 hour on ice in the dark. A final wash was performed with flow buffer and the phosphorylation status of AKT was acquired on the BD Fortessa LSRII and analyzed with FlowJo V.10.

Reverse transcriptase quantitative PCR

MDSCs were diluted to a concentration of 1×106 cells/mL in the presence or absence of 1 µM IPI-549 (Selleckchem #S8330) for 24 hours at 37°C. 2×10^6 MDSCs were used for RNA extraction using the RNeasy Plus Kit (Qiagen #4134), according to the manufacturer's protocol. Extracted RNA was quantified on the Thermo Scientific NanoDrop One Spectrophotometer. Complementary DNA (cDNA) was prepared using 1 µg RNA with the Applied Biosystems High-Capacity cDNA Reverse Transcription Kit with RNase Inhibitor (Thermo Fisher Scientific #4374966), according to the manufacturer's protocol. PCR primers were titrated, and optimal melting temperature was determined by preliminary melt curve experiment. Sybr green-based quantitative PCR was performed using human primers to *Arg1, Ccl2, Il10, Il6, Tgfb, Il1b, Il12b, Tbp* and *Tnfa*, using the SsoAdvanced Universal SYBR Green Supermix (Bio-Rad #1725271). mRNA levels were normalized to *Tbp* ($\Delta Ct = Ct^{\text{gene of interest}} - Ct^{Tbp}$). mRNA expression was normalized to baseline samples ($\Delta\Delta Ct = 2^{\wedge} - (\Delta Ct^{\text{sample}} - \Delta Ct^{\text{baseline}})$).

Murine studies

All C57Bl/6 mice were purchased from Charles River Laboratories (Wilmington, Virginia, USA) and housed

under strict pathogen-free conditions at the University of Ottawa Animal Care and Veterinary Services facility (Ottawa, Ontario, Canada). Murine protocols complied with the Canadian Council on Animal Care guidelines and were approved by the University of Ottawa Animal Care Committee ("Murine Models of Surgical Stress and Metastases", Protocol #4433) prior to initiating experiments.

In vivo, formulations for TG100-115 were prepared at 3 mg/kg or 6 mg/kg of body weight in PBS with 30% (v/v) PEG-300 (Sigma-Aldrich #8.07484). IPI-549 was prepared at 15 mg/kg or 30 mg/kg of body weight in PBS with 40% (v/v) PEG-400 (Sigma-Aldrich #25322-68-3). Formulations were prepared fresh, and mice were treated daily from 1 day before surgery (day −1) up to POD1. IPI-549 was administered by oral gavage two times a day while TG100-115 was administered once daily intraperitoneally. 200 µL of either formulation was administered.

Murine surgical stress model

Murine surgical stress was induced by performing a laparotomy and invasive left nephrectomy followed by abdominal closure using 5–0 Polysorb suture (Covidien #SL5687G) and skin staples as previously described.[12 13] On POD1 or POD3, the mice were sacrificed by lethal buprenorphine intraperitoneal (IP) injection at 0.1 mg/kg body weight, followed by cervical dislocation. Spleens were harvested via the left upper quadrant abdominal incision and splenocytes were dissociated through sterile 70 µm Cell Strainers (Thermo Fisher Scientific #08-771-2). Splenocytes were washed once in cRPMI, counted, and used for subsequent experiments.

Murine MDSC suppression assay

Sx-MDSCs were isolated using the MDSC Isolation Kit (Miltenyi #130-094-538) from surgically stressed mice on POD1. NK cells from no surgery control mice were isolated using the EasySep NK Isolation Kit (STEMCELL #100–0960). NK cells and Sx-MDSCs were co-cultured overnight in the presence of 100 U/mL of recombinant IL-2 (Thermo Fisher Scientific #CB-40043). YAC-1 cells were stained with CP450 and used as targets for the NK cells.

Assessment of postoperative metastases

B16F10-LacZ melanoma cells (3×10^5 cells, minimum 90% viability) were injected via intravenous tail vein into C57Bl/6 mice. 3 days following the tumor challenge, our standardized LacZ staining protocol was used for lung metastases.[12] On the first day, lungs were washed two times in Wash Buffer (1M magnesium chloride, 1% deoxycholate, 2% non-idet-P40, 0.1M sodium phosphate buffer pH 7.3), and then stained overnight at 37°C with X-Gal (Thermo Fisher Scientific #R0404) solution, 25 mg/mL in dimethylsulfoxide. The next day, lungs were washed two times with Wash Buffer and incubated for 24 hours at 4°C. On the third day, lungs were transferred into 10% buffered formalin for permanent fixation. Lungs were imaged using the Axiovision software V.4.8 (Zeiss) on the Zeiss SteREO Discovery Modular Microscope (Zeiss). From these electronic images, lung metastases were quantified using Fiji ImageJ.

MDSC adoptive transfer

To assess the effects of MDSC-specific inhibition of PI3K-γ, we used an MDSC adoptive transfer method.[13] In this study, MDSC-donor mice received TG100-115, IPI-549, or no treatment (n=8 per group), 1 day after surgery. Additionally, there was an MDSC-donor group that did not receive treatment or surgery. On POD1, MDSCs were isolated and resuspended to 1×10^7 cells/mL concentration. Next, 5×10^6 isolated MDSCs were adoptively transferred to each MDSC-recipient mice from their respective MDSC-donor experimental group, except for the no-transfer control group. 1 hour after the adoptive MDSC transfer, MDSC-recipient mice were tumor challenged with B16F10-LacZ, and lung metastases were counted on day 3.

Statistical analysis

Statistical analysis was performed in GraphPad Prism V.8. Unpaired, non-parametric Mann-Whitney U test was used when comparing two groups and paired Wilcoxon rank-sum test was used to compare two matched samples (ie, baseline vs POD1). Multiple comparisons were tested with non-parametric Kruskal-Wallis tests. P values were considered significant when $p<0.05$. Bonferroni corrections were applied when multiple queries were applied to a data set.

Author affiliations
[1]Cancer Research Program, The Ottawa Hospital Research Institute, Ottawa, Ontario, Canada
[2]University of Ottawa Department of Biochemistry Microbiology and Immunology, Ottawa, Ontario, Canada
[3]University of Ottawa Department of Cellular and Molecular Medicine, Ottawa, Ontario, Canada
[4]University of Ottawa Faculty of Medicine, Ottawa, Ontario, Canada
[5]adMare Bioinnovations, Vancouver, British Columbia, Canada

Acknowledgements We would like to thank Juliana Ng, Ahwon Jeong, and Marlena Scaffidi for enrolling and scheduling patients into this study. We thank Elaine Rose for helping in optimizing the Giemsa Wright staining protocol. Special thanks to Anna Von Rossum for their collaboration throughout the project.

Contributors Conceptualization: RA, MK, LA, GT. Methodology: LA, GT, DC, ABM, MM, CTS, EC, MK, RA, IS. Investigation: RA, LA, GT. Funding acquisition: RA. Supervision: RA, MK. Writing—original draft: LA, GT, DC, RA. Writing—review and editing: NK, MA, BV, MK, RA. Guarantor: RA.

Funding This work was supported by grants from the Department of Surgery, University of Ottawa (#N/A, RA), Canadian Institute of Health Research (#PJT 165807; RA), the Cancer Research Society (#707403; RA) and the Terry Fox Research Institute (#1073, RA). The Ottawa Hospital Academic Medical Organization (RA) provided funding for the Phase II clinical trial.

Competing interests EC and IS: adMare Bioinnovations supplied the compound library used for the small-molecule screen. MA: reported grants from Dragonfly Therapeutics and Actym Therapeutics as well as consulting compensations from Ahaka Biologics; all relationships are outside the submitted work. LA, GT, DC, ABM, MM, CS, NK, BV, MK, and RA declare no competing interests. The funders and commercial entities listed above had no role in study design; data collection, analysis, or interpretation; manuscript preparation; or the decision to submit the article for publication.

Patient consent for publication Not applicable.

Ethics approval This study involves human participants and was approved by (1) Ottawa Health Science Network Research Ethics Board #2011884-01H and (2) Ottawa Health Science Network Research Ethics Board #20160732-01H. Participants gave informed consent to participate in the study before taking part.

Provenance and peer review Not commissioned; externally peer reviewed.

Data availability statement Data are available upon reasonable request. All data relevant to the study are included in the article or uploaded as supplementary information.

ORCID iDs
Leonard Angka https://orcid.org/0000-0001-8324-6054
Gayashan Tennakoon https://orcid.org/0000-0003-3258-5771
Marisa Market https://orcid.org/0000-0002-3103-6765
Natasha Kekre https://orcid.org/0000-0001-8394-0855
Michele Ardolino https://orcid.org/0000-0003-4114-0985
Barbara C Vanderhyden https://orcid.org/0000-0002-7644-7189
Rebecca C Auer https://orcid.org/0000-0002-3617-0015

REFERENCES

1 Feng Q, Ni C, Zhou F, *et al*. Clinical relevance of perioperative changes in circulating tumor cells in resectable colorectal cancer. *BMC Cancer* 2025;25:1689.
2 Chen Z, Zhang P, Xu Y, *et al*. Surgical stress and cancer progression: the twisted tango. *Mol Cancer* 2019;18:132.
3 Huber-Lang M, Lambris JD, Ward PA. Innate immune responses to trauma. *Nat Immunol* 2018;19:327–41.
4 Loftus TJ, Mohr AM, Moldawer LL. Dysregulated myelopoiesis and hematopoietic function following acute physiologic insult. *Curr Opin Hematol* 2018;25:37–43.
5 Wang J, Su X, Yang L, *et al*. The influence of myeloid-derived suppressor cells on angiogenesis and tumor growth after cancer surgery. *Int J Cancer* 2016;138:2688–99.
6 Wang J, Yang L, Yu L, *et al*. Surgery-induced monocytic myeloid-derived suppressor cells expand regulatory T cells in lung cancer. *Oncotarget* 2017;8:17050–8.
7 Tang F, Tie Y, Hong W, *et al*. Targeting Myeloid-Derived Suppressor Cells for Premetastatic Niche Disruption After Tumor Resection. *Ann Surg Oncol* 2021;28:4030–48.
8 López-Soto A, Gonzalez S, Smyth MJ, *et al*. Control of Metastasis by NK Cells. *Cancer Cell* 2017;32:135–54.
9 Angka L, Martel AB, Kilgour M, *et al*. Natural Killer Cell IFNγ Secretion is Profoundly Suppressed Following Colorectal Cancer Surgery. *Ann Surg Oncol* 2018;25:3747–54.
10 Hiller JG, Perry NJ, Poulogiannis G, *et al*. Perioperative events influence cancer recurrence risk after surgery. *Nat Rev Clin Oncol* 2018;15:205–18.
11 Matzner P, Sandbank E, Neeman E, *et al*. Harnessing cancer immunotherapy during the unexploited immediate perioperative period. *Nat Rev Clin Oncol* 2020;17:313–26.
12 Tai L-H, de Souza CT, Bélanger S, *et al*. Preventing postoperative metastatic disease by inhibiting surgery-induced dysfunction in natural killer cells. *Cancer Res* 2013;73:97–107.
13 Tai L-H, Alkayyal AA, Leslie AL, *et al*. Phosphodiesterase-5 inhibition reduces postoperative metastatic disease by targeting surgery-induced myeloid derived suppressor cell-dependent inhibition of Natural Killer cell cytotoxicity. *Oncoimmunology* 2018;7:e1431082.
14 Angka L, Tanese de Souza C, Baxter KE, *et al*. Perioperative arginine prevents metastases by accelerating natural killer cell recovery after surgery. *Mol Ther* 2022;30:3270–83.
15 Mandruzzato S, Brandau S, Britten CM, *et al*. Toward harmonized phenotyping of human myeloid-derived suppressor cells by flow cytometry: results from an interim study. *Cancer Immunol Immunother* 2016;65:161–9.
16 Veglia F, Sanseviero E, Gabrilovich DI. Myeloid-derived suppressor cells in the era of increasing myeloid cell diversity. *Nat Rev Immunol* 2021;21:485–98.
17 Condamine T, Dominguez GA, Youn J-I, *et al*. Lectin-type oxidized LDL receptor-1 distinguishes population of human polymorphonuclear myeloid-derived suppressor cells in cancer patients. *Sci Immunol* 2016;1:aaf8943.
18 ElTanbouly MA, Croteau W, Noelle RJ, *et al*. VISTA: a novel immunotherapy target for normalizing innate and adaptive immunity. *Semin Immunol* 2019;42:101308.
19 Davis RJ, Moore EC, Clavijo PE, *et al*. Anti-PD-L1 Efficacy Can Be Enhanced by Inhibition of Myeloid-Derived Suppressor Cells with a Selective Inhibitor of PI3Kδ/γ. *Cancer Res* 2017;77:2607–19.
20 Crowell HL, Soneson C, Germain P-L, *et al*. On the discovery of subpopulation-specific state transitions from multi-sample multi-condition single-cell rna sequencing data. *Bioinformatics* [Preprint] 2019.
21 Liberzon A, Subramanian A, Pinchback R, *et al*. Molecular signatures database (MSigDB) 3.0. *Bioinformatics* 2011;27:1739–40.
22 Liberzon A, Birger C, Thorvaldsdóttir H, *et al*. The Molecular Signatures Database (MSigDB) hallmark gene set collection. *Cell Syst* 2015;1:417–25.
23 Trovato R, Fiore A, Sartori S, *et al*. Immunosuppression by monocytic myeloid-derived suppressor cells in patients with pancreatic ductal carcinoma is orchestrated by STAT3. *J Immunother Cancer* 2019;7:255.
24 Gaudillière B, Fragiadakis GK, Bruggner RV, *et al*. Clinical recovery from surgery correlates with single-cell immune signatures. *Sci Transl Med* 2014;6:255ra131.
25 Kotliar D, Veres A, Nagy MA, *et al*. Identifying gene expression programs of cell-type identity and cellular activity with single-cell RNA-Seq. *Elife* 2019;8:e43803.
26 Alshetaiwi H, Pervolarakis N, McIntyre LL, *et al*. Defining the emergence of myeloid-derived suppressor cells in breast cancer using single-cell transcriptomics. *Sci Immunol* 2020;5:eaay6017.
27 Kim Y-S, Kim Y-J, Lee J-M, *et al*. Functional changes in myeloid-derived suppressor cells (MDSCs) during tumor growth: FKBP51 contributes to the regulation of the immunosuppressive function of MDSCs. *J Immunol* 2012;188:4226–34.
28 Ku AW, Muhitch JB, Powers CA, *et al*. Tumor-induced MDSC act via remote control to inhibit L-selectin-dependent adaptive immunity in lymph nodes. *Elife* 2016;5:e17375.
29 Zanzinger K, Schellack C, Nausch N, *et al*. Regulation of triggering receptor expressed on myeloid cells 1 expression on mouse inflammatory monocytes. *Immunology* 2009;128:185–95.
30 Condamine T, Mastio J, Gabrilovich DI. Transcriptional regulation of myeloid-derived suppressor cells. *J Leukoc Biol* 2015;98:913–22.
31 Kaneda MM, Messer KS, Ralainirina N, *et al*. PI3Kγ is a molecular switch that controls immune suppression. *Nature* 2016;539:437–42.
32 De Henau O, Rausch M, Winkler D, *et al*. Overcoming resistance to checkpoint blockade therapy by targeting PI3Kγ in myeloid cells. *Nature* 2016;539:443–7.
33 Zhang X, Shen L, Liu Q, *et al*. Inhibiting PI3 kinase-γ in both myeloid and plasma cells remodels the suppressive tumor microenvironment in desmoplastic tumors. *J Control Release* 2019;309:173–80.
34 Chan G, Bivins-Smith ER, Smith MS, *et al*. Transcriptome analysis of NF-kappaB- and phosphatidylinositol 3-kinase-regulated genes in human cytomegalovirus-infected monocytes. *J Virol* 2008;82:1040–6.
35 Saudemont A, Garçon F, Yadi H, *et al*. p110gamma and p110delta isoforms of phosphoinositide 3-kinase differentially regulate natural killer cell migration in health and disease. *Proc Natl Acad Sci U S A* 2009;106:5795–800.
36 Mace EM. Phosphoinositide-3-Kinase Signaling in Human Natural Killer Cells: New Insights from Primary Immunodeficiency. *Front Immunol* 2018;9:445.
37 Uchida A, Kolb R, Micksche M. Generation of suppressor cells for natural killer activity in cancer patients after surgery. *J Natl Cancer Inst* 1982;68:735–41.
38 Weber R, Fleming V, Hu X, *et al*. Myeloid-Derived Suppressor Cells Hinder the Anti-Cancer Activity of Immune Checkpoint Inhibitors. *Front Immunol* 2018;9:1310.
39 Grauers Wiktorin H, Aydin E, Kiffin R, *et al*. Impact of Surgery-Induced Myeloid-derived Suppressor Cells and the NOX2/ROS Axis on Postoperative Survival in Human Pancreatic Cancer. *Cancer Res Commun* 2024;4:1135–49.

40 Zindel J, Kubes P. DAMPs, PAMPs, and LAMPs in Immunity and Sterile Inflammation. *Annu Rev Pathol* 2020;15:493–518.
41 Gao X-H, Tian L, Wu J, *et al*. Circulating $CD14^{+}$ $HLA\text{-}DR^{-/low}$ myeloid-derived suppressor cells predicted early recurrence of hepatocellular carcinoma after surgery. *Hepatol Res* 2017;47:1061–71.
42 Ostrand-Rosenberg S, Fenselau C. Myeloid-Derived Suppressor Cells: Immune-Suppressive Cells That Impair Antitumor Immunity and Are Sculpted by Their Environment. *J Immunol* 2018;200:422–31.
43 van Wigcheren GF, Cuenca-Escalona J, Stelloo S, *et al*. Myeloid-derived suppressor cells and tolerogenic dendritic cells are distinctively induced by PI3K and Wnt signaling pathways. *J Biol Chem* 2023;299:105276.
44 Isoyama S, Mori S, Sugiyama D, *et al*. Cancer immunotherapy with PI3K and PD-1 dual-blockade via optimal modulation of T cell activation signal. *J Immunother Cancer* 2021;9:e002279.
45 Dreyling M, Santoro A, Mollica L, *et al*. Long-term safety and efficacy of the PI3K inhibitor copanlisib in patients with relapsed or refractory indolent lymphoma: 2-year follow-up of the CHRONOS-1 study. *Am J Hematol* 2020;95:362–71.
46 Tie J, Cohen JD, Lahouel K, *et al*. Circulating Tumor DNA Analysis Guiding Adjuvant Therapy in Stage II Colon Cancer. *N Engl J Med* 2022;386:2261–72.
47 The TRACERx consortium, Abbosh C, The PEACE consortium, *et al*. Phylogenetic ctDNA analysis depicts early-stage lung cancer evolution. *Nature* 2017;545:446–51.
48 Garcia-Murillas I, Schiavon G, Weigelt B, *et al*. Mutation tracking in circulating tumor DNA predicts relapse in early breast cancer. *Sci Transl Med* 2015;7:302ra133.
49 Angka L, Martel AB, Ng J, *et al*. A Translational Randomized Trial of Perioperative Arginine Immunonutrition on Natural Killer Cell Function in Colorectal Cancer Surgery Patients. *Ann Surg Oncol* 2022;29:7410–20.
50 Stuart T, Butler A, Hoffman P, *et al*. Comprehensive Integration of Single-Cell Data. *Cell* 2019;177:1888–902.
51 Hafemeister C, Satija R. Normalization and variance stabilization of single-cell RNA-seq data using regularized negative binomial regression. *Genome Biol* 2019;20:296.
52 Schubert M, Klinger B, Klünemann M, *et al*. Perturbation-response genes reveal signaling footprints in cancer gene expression. *Nat Commun* 2018;9:20.
53 DeTomaso D, Jones MG, Subramaniam M, *et al*. Functional interpretation of single cell similarity maps. *Nat Commun* 2019;10:4376.